Self-organized aggregation and traveling wave in a kinetic transport model for run-and-tumble bacteria

Shugo YASUDA *

Graduate School of Information Science,

University of Hyogo, Kobe 650-0047, Japan.

Abstract

The self-organized pattern formation of run-and-tumble chemotactic bacteria is numerically investigated based on a kinetic transport equation considering internal adaptation dynamics and a finite tumbling duration. It is confirmed that the volcano-like aggregation profile is generated due to the coupling of diffusion and internal adaptation dynamics occurring at a large adaptation-time scaling. Moreover, an extended Keller-Segel model, derived by the asymptotic analysis of the kinetic model at the large adaptation-time scale, can describe the volcano effect well. It is also found that when the mean run length of the bacteria becomes large, the volcano effect is more enhanced and unexpectedly, different types of pattern formation (i.e., standing and traveling bands) arise at very large adaptation times. The mathematical mechanism of the novel pattern formation should be an important future study. This paper is a resume of previous studies by the author in *S. Yasuda, Bull. Math. Biol.* ***84****, 113 (2022)* and *K. Adachi and S. Yasuda, Springer Proc. Math. Stat.* ***429****, 235 (2023).*

Keywords: Kinetic transport equation, chemotaxis, run-and-tumble, pattern formation, Monte Carlo simulation

* Electronic mail: yasuda@gsis.u-hyogo.ac.jp

I. INTRODUCTION

Collective motion of chemotactic bacteria, such as *E. Coli*, relies on, at the individual level, a continuous reorientation by alternating runs and tumbles [1, 14]. It has been established that the bacteria modulate the run length according to a temporal sensing of extracellular chemical cues via an intracellular signal transduction. This chemotactic behavior can be described by a kinetic transport equation with a scattering kernel describing the velocity jump process in the run-and-tumble motion of the bacteria [4, 5, 7, 9, 11, 16].

Kinetic transport equations have been successfully utilized to elucidate the mathematics and physics behind the collective motions of bacteria such as the traveling pulse in the microchannel [6, 21], the concentric pattern formation of engineered *E. Coli* [25], and the volcano-like aggregation profile observed in microscale aggregation [15]. This paper concerns the self-organized aggregation of chemotactic bacteria, such as the volcano effect (i.e., the bimodal aggregation of chemotactic bacteria), which was first observed in an experiment of microscale aggregation of *E. Coli* [15].

Recently, we investigated the microscale aggregation of chemotactic bacteria based on the kinetic transport model [27–29]. In Ref. [27], the occurrence of the self-organized aggregation was investigated numerically based on a kinetic transport equation with an internal state, and the effect of internal adaptation on the self-organized aggregation was clarified. An important finding of Ref. [27] is the occurrence of the plateau (or trapezoidal) profile in the chemotactic aggregation at a large adaptation-time regime. In Ref. [28], the aggregation of chemotactic bacteria under a given background concentration of chemical cue was investigated based on a kinetic transport equation considering the non-instantaneous tumbling process, where the interaction between two different populations of running and tumbling cells is considered. It was clarified that the volcano effect occurs due to the coupling of diffusion, adaptation, and finite tumbling duration at the large adaptation-time scaling. Furthermore, in Ref. [29], the volcano effect was also confirmed in self-organized aggregations by the numerical analysis of the kinetic transport equation in a two-dimensional square periodic domain. Remarkably, the numerical simulations also discovered novel types of self-organized pattern formation (i.e., standing and traveling bands).

This paper is a resume of the previous studies. The rest of the paper is organized as follows: In Sec. 2, we present the problem and the formulation of the kinetic transport

equation. In Sec. 3, the continuum-limit equations are derived from the kinetic transport equation. In Sec. 4, the numerical results obtained by Monte Carlo simulations based on the kinetic transport equation are presented. In Sec. 4, we offer concluding remarks and some future perspectives.

II. PROBLEM AND FORMULATION

A. Problem

We consider the chemotactic bacteria in the two-dimensional space, $x \in [0, L] \times [0, L]$ with the periodic boundary condition. Initially, at time t=0, the bacteria are spatially uniformly distributed with random velocities with a constant speed $|v| = \mathrm{v_c}$. Hereafter, the subscript "c" represents the characteristic quantities, which are used to nondimensionalize the basic equations. The external chemical cue is also uniformly distributed at time $t = 0$.

The bacteria sense the temporal variation of the external chemical cue via their intracellular signal transduction, which will be described in the next subsection, and create a biased random motion toward the higher concentration of the chemical cue. Moreover, the bacteria produce the chemical cue by themselves.

Thus, the bacteria are more likely to migrate to a location with a higher concentration of chemical cues, and then the concentration of chemical cues at the location further increases due to the self-production of chemical cues by the bacteria population. This positive feedback triggers self-organized pattern formation. We will numerically investigate the self-organized pattern formation under a variation of the parameters related to the chemotactic response of the bacteria.

B. Kinetic Transport Model for Chemotactic Bacteria

As previously mentioned, the collective motion of the chemotactic bacteria stems, at the individual level, from biased random motion by alternating runs and tumbles, where the length of the run is determined via intracellular signal transduction. Although intracellular signal transduction is very complicated in general, the fundamental property necessary for the chemotactic response is described by the excitation and adaptation dynamics of the

internal state of the bacteria [7, 23]. In the present paper, we only consider the following simple adaptation dynamics of the internal state $m \in \mathbb{R}$:

$$\dot{m} = \frac{M(S) - m}{\tau}, \tag{1}$$

where τ is the adaptation time and $M(S)$ denotes the local equilibrium of the internal state at the concentration of the external chemical cue S.

The modulation of the run length is determined by the deviation of the current internal state m from the local equilibrium state $M(S)$, i.e., $|M(S) - m|$. We consider the following modulation function for the tumbling frequency:

$$\Lambda_\delta(M(S) - m) = 1 - F\left(\frac{M(S) - m}{\delta}\right), \tag{2}$$

where δ denotes the stiffness of the chemotactic response and the response function $F(X)$ has the following property:

$$F(0) = 0, \quad F'(X) > 0, \quad F(X \to \pm\infty) = \pm\chi,$$

where χ ($0<\chi<1$) represents the modulation amplitude. In this study, we consider the following form:

$$F(X) = \frac{\chi X}{\sqrt{1 + X^2}}. \tag{3}$$

For the local equilibrium of the internal state, we consider the following formula:

$$M(S) = \log(S). \tag{4}$$

This formula comes from the well-known logarithmic sensing of *E. coli* [10].

The bacteria alternate runs and tumbles. We write the frequency when the running cells change to the tumbling cells as $\lambda\Lambda_\delta(M(S) - m)$ and the frequency when the tumbling cells change to the running cells as $\mu > 0$. Here, $\lambda > 0$ is the mean tumbling frequency of the bacteria when their internal state is in local equilibrium, i.e., $m = M(S)$.

Then, when we write the population density of running cells with a velocity $v \in [v, v+dv]$ and an internal state $m \in [m, m + dm]$ at time $t > 0$ and at space $x \in R^d$ (where d is the dimension of space) as $d\rho_f = f(t, x, v, m)dvdm$ and that of the tumbling cells with an internal state $m \in [m, m + dm]$ as $d\rho_g = g(t, x, m)dm$, the time evolution of the densities $f(t, x, v, m)$ and $g(t, x, m)$ is described as follows:

$$\partial_t f + v \cdot \nabla_x f + \partial_m \left\{ \left(\frac{M(S) - m}{\tau}\right) f \right\} = \mu \frac{g}{||V||} - \lambda\Lambda_\delta(M(S) - m)f \tag{5a}$$

$$\partial_t g + \partial_m \left\{ \left(\frac{M(S) - m}{\tau} \right) g \right\} = \lambda \Lambda_\delta (M(S) - m) \int_V f(t, x, v, m) dv - \mu g, \tag{5b}$$

where $||V||$ is the volume of the velocity space, i.e., $||V|| = \int_V dv$, and the velocity space is the surface of the ball (i.e., $V = \mathrm{v_c} \mathbb{S}^d$).

The total population density ρ, the population density of running cells ρ_f, and the population density of tumbling cells ρ_g are given as follows:

$$\rho(t, x) = \rho_f(t, x) + \rho_g(t, x), \tag{6a}$$

$$\rho_f(t, x) = \int_{\mathbb{R}} \int_V f(t, x, v, m) dv dm, \tag{6b}$$

$$\rho_g(t, x) = \int_{\mathbb{R}} g(t, x, m) dm. \tag{6c}$$

Since we consider the self-organized pattern formation, the kinetic transport equation (5) is coupled with the reaction-diffusion equation of the chemical cue $S(t, x)$, i.e.,

$$\partial_t S = D_S \Delta_x S - aS + b\rho, \tag{7}$$

where D_S is the diffusion constant, a is the degradation rate of the chemical cue, and b is the production rate of the chemical cue by the bacteria.

C. Nondimensionalization

We introduce the nondimensional quantities as follows:

$$\hat{f} = f/(\rho_\mathrm{c}/||V||), \quad \hat{g} = g/\rho_\mathrm{c}, \quad \hat{t} = t/\mathrm{t_c}, \quad \hat{x} = x/\mathrm{L_c}, \quad \hat{v} = v/\mathrm{v_c}. \tag{8}$$

Then, the kinetic transport equation (5) can be written as follows:

$$\sigma \partial_{\hat{t}} \hat{f} + \hat{v} \cdot \nabla_{\hat{x}} \hat{f} + \partial_m \left\{ \left(\frac{M(S) - m}{\hat{\tau}} \right) \hat{f} \right\} = \frac{1}{\varepsilon} \left[\hat{\mu} \hat{g} - \Lambda_\delta (M(S) - m) \hat{f} \right], \tag{9a}$$

$$\sigma \partial_{\hat{t}} \hat{g} + \partial_m \left\{ \left(\frac{M(S) - m}{\hat{\tau}} \right) \hat{g} \right\} = \frac{1}{\varepsilon} \left[\Lambda_\delta (M(S) - m) < \hat{f} > - \hat{\mu} \hat{g} \right], \tag{9b}$$

where $< \hat{f} >$ is the average of $\hat{f}$ over the velocity space $\hat{V}$, which is defined as

$$< f >= \frac{1}{||\hat{V}||} \int_{\hat{V}} f(\hat{t}, \hat{x}, \hat{v}, m) d\hat{v}, \tag{10}$$

with $||\hat{V}|| = \int_{\hat{V}} d\hat{v}$. In Eq. (9), we have also introduced the following nondimensional parameters:

$$\sigma = \mathrm{L_c}/(\mathrm{v_c t_c}), \quad \varepsilon = \mathrm{v_c}/(\lambda \mathrm{L_c}), \quad \hat{\tau} = \tau/(\mathrm{L_c}/\mathrm{v_c}), \quad \hat{\mu} = \mu/\lambda. \tag{11}$$

Here, σ is the time parameter, ε is the mean run length at the reference state, $\hat{\tau}$ is the non-dimensional adaptation time, and $\hat{\mu}$ is the ratio of the mean run duration to the mean tumbling duration.

The population densities defined in Eq. (6) are written as follows:

$$\hat{\rho}(\hat{t}, \hat{x}) = \hat{\rho}_f(\hat{t}, \hat{x}) + \hat{\rho}_g(\hat{t}, \hat{x}), \tag{12a}$$

$$\hat{\rho}_f(\hat{t}, \hat{x}) = \int_{\mathbb{R}} < \hat{f} > (\hat{t}, \hat{x}, m) dm, \tag{12b}$$

$$\hat{\rho}_g(\hat{t}, \hat{x}) = \int_{\mathbb{R}} \hat{g}(\hat{t}, \hat{x}, m) dm. \tag{12c}$$

We note that when taking the small tumbling duration limit $\hat{\nu} = \hat{\mu}^{-1} \to 0$, the density of tumbling cells $\hat{g}$ becomes $\hat{g} \to 0$, and thus, Eq. (9) is reduced as follows:

$$\sigma \partial_t \hat{f} + v \cdot \nabla_x \hat{f} + \partial_m \left\{ \left(\frac{M(S) - m}{\hat{\tau}} \right) \hat{f} \right\} = \frac{1}{\varepsilon} \Lambda_\delta (M(S) - m) \left(< \hat{f} > - \hat{f} \right). \tag{13}$$

The reaction-diffusion equation (7) is nondimensionalized as follows:

$$\sigma_S \partial_{\hat{t}} \hat{S} = \hat{D}_S \Delta_{\hat{x}} \hat{S} - \hat{S} + \hat{\rho}, \tag{14}$$

where σ_S, $\hat{S}$, and $\hat{D}_S$ are defined as follows:

$$\sigma_S = 1/(a \mathrm{t_c}), \quad \hat{S} = S/(b \rho_\mathrm{c}/a), \quad \hat{D}_S = D_S/(a \mathrm{L_c^2}).$$

In the following text, we fix $\hat{D}_S = 1$. This indicates that the characteristic length L_c is defined as $L_c = \sqrt{D_S/a}$.

III. CONTINUUM-LIMIT EQUATIONS

It has been proved that different types of continuum-limit (i.e., $\varepsilon \to 0$) equations are obtained by the asymptotic analysis of the kinetic transport equation at different scalings of the adaptation time [7, 17, 19, 25]. In this study, we utilize the continuum-limit equations to confirm the asymptotic behaviors of the MC simulations of the kinetic transport equation

(9), which will be given in the next section. In this section, we summarize the continuum-limit equations obtained at two different scalings of the adaptation time. An asymptotic relation between the two different continuum-limit equations is also briefly explained.

We consider small and large adaptation-time scalings, i.e., $\hat{\tau} = O(\varepsilon)$ and $\hat{\tau} = O(1/\varepsilon)$, respectively. We also consider the diffusive time scale $\sigma = \varepsilon$. These settings of the time scale parameters are physically interpreted as follows: The time scale parameter $\sigma = \varepsilon$ reads that the characteristic time $t_{\rm c}$ corresponds to the diffusion time of the population density, i.e., $t_{\rm c} = t_d$, where the diffusion time t_d is defined as

$$t_d = L_{\rm c}^2 / D_\rho \tag{15}$$

with the diffusion constant defined as $D_\rho = {\rm v_c}^2/\lambda$. The small adaptation time scaling $\hat{\tau} = O(\varepsilon)$ indicates that the adaptation time is comparable to the running duration (i.e., $\tau \sim \lambda^{-1}$), while the large adaptation-time scaling $\hat{\tau} = O(1/\varepsilon)$ indicates that the adaptation time is comparable to the diffusion time (i.e., $\tau \sim t_d$).

In the following, we only consider the case where the stiffness of the modulation function is independent on ε and $\delta = O(1)$ in Eq. (2) (although the stiff chemotactic response, such as those considered in the previous studies [17, 19, 20] are more realistic in general).

In the following of the text, we write the nondimensional quantities without " ˆ " for simplicity unless otherwise stated.

A. Small adaptation-time scaling

We consider the small adaptation-time scaling in Eq. (9) as follows:

$$\tau = \alpha\varepsilon, \quad \sigma = \varepsilon, \tag{16}$$

where the parameter $\alpha = O(1)$ denotes the ratio of the adaptation time to the mean running duration (i.e., $\alpha = \tau/\lambda^{-1}$).

Then, Eq. (9) is written as follows:

$$\varepsilon^2 \partial_t f_\varepsilon + \varepsilon v \cdot \nabla_x f_\varepsilon + \partial_m \left\{ \left(\frac{M_\varepsilon - m}{\alpha} \right) f_\varepsilon \right\} = \mu g_\varepsilon - \Lambda(M_\varepsilon - m) f_\varepsilon, \tag{17a}$$

$$\varepsilon^2 \partial_t g_\varepsilon + \partial_m \left\{ \left(\frac{M_\varepsilon - m}{\alpha} \right) g_\varepsilon \right\} = \Lambda(M_\varepsilon - m) < f_\varepsilon > - \mu g_\varepsilon, \tag{17b}$$

where the subscript ε represents the expansion of the quantity with respect to ε, e.g., $f_\varepsilon = f_0 + \varepsilon f_1 + \varepsilon^2 f_2 \cdots$. Here, we also write $M(S_\varepsilon)$ as $M_\varepsilon = M(S_\varepsilon) = M_0 + \varepsilon M_1 + \cdots$.

The asymptotic analysis of the above equation gives the following standard KS equation for the total population density ρ at the continuum limit $\varepsilon \to 0$ as follows:

$$\sigma_\nu \partial_t \rho_0 - \nabla_x \cdot c_d \left[\nabla_x \rho_0 + \frac{\Lambda'(0)\alpha\rho_0}{1+\alpha} \nabla_x M_0 \right] = 0, \tag{18}$$

where σ_ν is the time-scale parameter defined as $\sigma_\nu = 1 + \nu$ and c_d is the diffusion constant calculated as $c_d = 1/d$ for $d = 1$, 2, and 3. Here, we note again that the parameter $\nu = \mu^{-1}$ denotes the relative mean tumbling duration to the mean running duration. The population densities of the running and tumbling cells are obtained as follows:

$$\rho_f = \frac{1}{1+\nu}\rho_0, \quad \rho_g = \frac{\nu}{1+\nu}\rho_0. \tag{19}$$

The formal derivation of the KS equation (18) is concisely described in Appendix A 1.

Equation (18) shows that the tumbling duration ν only affects the time scale, but the spatial distribution of the population density ρ_0 in the steady state are not affected by the tumbling duration at the continuum limit $\varepsilon \to 0$ in the small adaptation-time scaling (16).

B. Large adaptation-time scaling

We consider the large adaptation time scaling at Eq. (9) as follows:

$$\tau = \beta/\varepsilon, \quad \sigma = \varepsilon, \tag{20}$$

where the parameter $\beta = O(1)$ denotes the ratio of the adaptation time to the diffusion time (i.e., $\beta = \tau_a/t_d$).

Then, Eq. (9) is written as follows:

$$\varepsilon^2 \partial_t f_\varepsilon + \varepsilon v \cdot \nabla_x f_\varepsilon + \varepsilon^2 \partial_m \left\{ \left(\frac{M_\varepsilon - m}{\beta} \right) f_\varepsilon \right\} = \mu g_\varepsilon - \Lambda(M_\varepsilon - m) f_\varepsilon, \tag{21a}$$

$$\varepsilon^2 \partial_t g_\varepsilon + \varepsilon^2 \partial_m \left\{ \left(\frac{M_\varepsilon - m}{\beta} \right) g_\varepsilon \right\} = \Lambda(M_\varepsilon - m) < f_\varepsilon > - \mu g_\varepsilon. \tag{21b}$$

The asymptotic analysis of Eq. (21) gives the continuum-limit equation at $\varepsilon \to 0$ as follows:

$$\partial_t h_0 - \nabla_x \cdot \left[\frac{c_d}{\Lambda(M_0 - m)} \nabla_x \left(\frac{h_0}{1 + \nu\Lambda(M_0 - m)} \right) \right] + \partial_m \left[\left(\frac{M_0 - m}{\beta} \right) h_0 \right] = 0, \tag{22}$$

where h_0 denotes the density of the cells with internal state m and is defined as follows:

$$h_0(t,x,m) =< f_0 > (t,x,m) + g_0(t,x,m).$$

Although the above continuum-limit equation (22) was previously derived in Ref. [25], we concisely describe the formal derivation of Eq. (22) in Appendix A 2 for the completeness of the present paper. We also remark that Eq. (22) with $\nu = 0$ was also derived in Ref. [27] from the kinetic transport equation without finite tumbling duration (13). However, interestingly, the volcano effect was not observed in the previous study while, as it will be seen in Sec. IV, the volcano effect arises both in MC simulations and numerical results of Eq. (22) with the finite tumbling duration $\nu \neq 0$. This indicates that the small modification introduced in Eq. (22) with the parameter ν enables to produce the volcano effect.

The total population density of cells $\rho_0(t,x)$ is given by the integration of h_0 with respect to the internal state m, i.e.,

$$\rho_0(t,x) = \int_{\mathrm{R}} h_0(t,x,m)dm.$$

In the following text, we call Eq. (22) the extended Keller-Segel (ExKS) model because the consistency with the standard Keller-Segel model is confirmed at $\beta \to 0$, as shown in the next subsection.

C. Consistency between the KS and ExKS models

It is easily seen that by taking the limit as $\alpha \to \infty$ in Eq. (18), the KS equation is written as follows:

$$\sigma_\mu \partial_t \rho_0 - \nabla_x \cdot c_d \left[\nabla_x \rho_0 + \Lambda'(0)\rho_0 \nabla_x M_0\right] = 0.$$

The same equation is also obtained by taking the limit $\beta \to 0$ in Eq. (22). This can be seen as follows:

When taking the limit $\beta \to 0$ at Eq. (22), we have the equation as follows:

$$\partial_m \left[(M_0 - m)h_0\right] = 0.$$

Thus, the solution h_0 at $\beta \to 0$ is written as follows:

$$h_0(t,x,m) = \rho_0(t,x)\delta(M_0 - m), \tag{23}$$

where $\delta(m)$ is the Dirac delta function.

On the other hand, by integrating Eq. (22) with respect to m, we obtain the equation as follows:

$$\partial_t \rho_0 - \nabla_x \cdot j_1 = 0, \tag{24}$$

where

$$j_1 = c_d \int_{\mathbb{R}} B_1(t, x, m) dm, \tag{25}$$

and B_1 is defined as Eq. (A.16b).

By substituting Eq. (23) into Eq. (A.16b), we obtain the equation as follows:

$$\begin{aligned} B_1 &= -\frac{\mu}{\Lambda(M_0 - m)} \nabla_x \left(\frac{\rho_0 \delta(M_0 - m)}{\mu + \Lambda(M_0 - m)} \right) \\ &= -\frac{\mu \delta(M_0 - m) \nabla_x \rho_0}{\Lambda(M_0 - m)(\mu + \Lambda(M_0 - m))} - \frac{\mu \rho_0 \nabla_x M_0}{\Lambda(M_0 - m)} \left[\frac{\delta'(M_0 - m)}{\mu + \Lambda(M_0 - m)} - \frac{\Lambda'(M_0 - m)\delta(M_0 - m)}{(\mu + \Lambda(M_0 - m))^2} \right]. \end{aligned} \tag{26}$$

Thus, the flux j_1 (Eq. (25)) at $\beta \to 0$ is written as follows:

$$\begin{aligned} j_1 &= -\frac{\mu c_d \nabla_x \rho_0}{\Lambda(0)(\mu + \Lambda(0))} - \mu c_d \rho_0 \nabla_x M_0 \left[\frac{\Lambda'(0)(\mu + \Lambda(0)) + \Lambda(0)\Lambda'(0)}{\Lambda^2(0)(\mu + \Lambda(0))^2} - \frac{\Lambda'(0)}{\Lambda(0)(\mu + \Lambda(0))^2} \right] \\ &= -\frac{\mu c_d}{\Lambda(0)(\mu + \Lambda(0))} \left[\nabla_x \rho_0 + \frac{\Lambda'(0)}{\Lambda(0)} \rho_0 \nabla_x M_0 \right]. \end{aligned} \tag{27}$$

By using $\Lambda(0) = 1$ and $\nu = \mu^{-1}$, it is seen that Eq. (24) with Eq. (27) provides the KS model at $\alpha \to \infty$. Due to this consistency, we can say that the ExKS model (22) is an extension of the standard KS model to involve the effects of the internal adaptation dynamics at the large adaptation-time scaling.

IV. NUMERICAL RESULTS

The kinetic transport equation (9) is numerically solved by the Monte Carlo method, which was developed in Refs. [26–28] (see, for example, appendix B in Ref. [28]). In the MC simulations, the two-dimensional periodic square domain $x \in [0, L] \times [0, L]$ is divided into $I \times I$ square lattice cells with $I = 50$ and, on average, two-thousand MC particles are distributed in each lattice cell (i.e., the total number of MC particles $N = 5 \times 10^6$). The concentration of chemical cue S is calculated by a standard finite-volume method over the lattice mesh system. The time-step size is set as $\Delta t = 2 \times 10^{-4}$.

We note that in the MC method, the characteristic time $\mathrm{t_c}$ is fixed as $\mathrm{t_c} = \mathrm{L_c}/\mathrm{v_c}$, which reads $\sigma = 1$ at Eq. (9), while the time period of the MC simulation is varied according to the value of ε as $0 \leq t \leq \frac{TL^2}{\varepsilon}$, where $T = 4$ is used unless otherwise stated. This large-time simulation allows comparing the MC results with the continuum-limit equations obtained at the diffusive scaling $\sigma = \varepsilon$. The MC results are also time-averaged over the time period $\delta t = \frac{0.1L^2}{\varepsilon}$.

As the initial condition, we consider the equilibrium solution of Eqs. (9) and (14), which is described as

$$f(0,x,v,m) = \frac{\mu\delta(m - M(S))}{1+\mu}, \quad g(0,x,m) = \frac{\delta(m - M(S))}{1+\mu}, \quad S(0,x) = 1.$$

More specifically, at time $t = 0$, the positions and velocities of MC particles are uniformly randomly distributed while their internal states are fixed as $m = 0$, which corresponds to the local equilibrium of the internal state described by Eq. (4) with $S = 1$.

Numerical simulations are performed for various values of the adaptation time τ, mean run length ε, stiffness δ, and modulation amplitude χ, while the spatial extent $L = 10$ and the relative tumbling duration $\mu^{-1} = 0.3$ are fixed.

A. Instability Diagram

Figure 1 shows the instability diagrams with respect to the relative adaptation time τ/ε and the stiffness χ/δ at different values of ε. Here, the two parameters τ/ε and χ/δ are chosen in the instability diagram since it is found in our previous studies [27, 28] that they are involved in the linear stability condition of the Keller-Segel (KS) model [12, 13] derived by the asymptotic analysis of the kinetic transport model (9) at the small adaptation-time scaling $\tau = O(\varepsilon)$. The linear stability condition of the KS model is written as

$$\frac{\chi}{\delta} \leq \frac{1+\alpha}{\alpha}(1 + D_S k^2), \tag{28}$$

where $\alpha = \tau/\varepsilon$ represents the relative adaptation time to the mean tumbling time and k is the Fourier mode of the density perturbation. The derivation of the above condition can be referred in Ref. [28]. In the diagram, the linear stability condition of the KS model is shown by the dashed lines in each figure.

It is seen that under the linear stability condition of the KS model, no pattern formations are observed both at ε =0.1 and $\varepsilon = 1$. Moreover, the linear stability condition of the KS

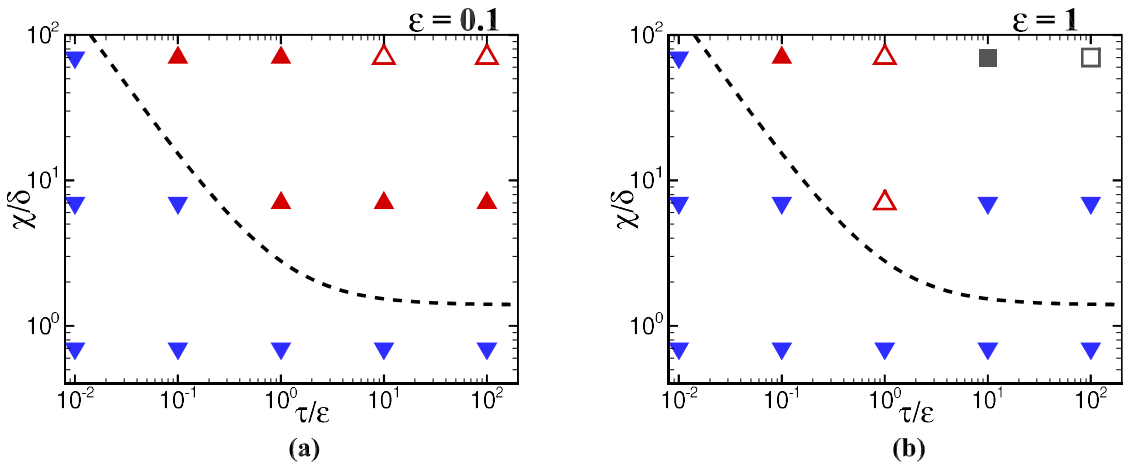

FIG. 1: Instability diagrams with respect to the relative adaptation time τ/ε and the stiffness χ/δ at $\varepsilon = 0.1$ [in (a)] and $\varepsilon = 1.0$ [in (b)]. (Reprinted from Fig. 1 in Ref. [29].) The modulation amplitude $\chi = 0.7$ is fixed. The closed downward triangles ▼ show the stability, where the maximum of the power spectra of total population density is smaller than 0.1, i.e., $\max_{k,l} |\tilde{\rho}_{k,l}|/I^2 < 0.1$, where $\tilde{\rho}_{k,l}$ is the discrete Fourier Transform of the total population density. The dashed line shows the linear stability condition of the Keller-Segel (KS) equation at the wave length L (i.e., Eq. (35) in Ref. [27] with $k = 2\pi/L$). The closed and open upward triangles, ▲ and △ show, respectively, the unimodal and volcano aggregation. The closed and open squares, ■ and □ show the standing and traveling band, respectively.

model is sharp at the small adaptation-time regime $\tau \lesssim O(\varepsilon)$, where the KS model is indeed relevant to the asymptotic solution of the kinetic transport equation (9). On the other hand, at the large adaptation-time regime $\tau = O(1/\varepsilon)$, instead of the usual KS model, an extended KS (ExKS) model (i.e., Eq. (17) in Ref. [28]) is obtained by the asymptotic analysis of Eq. (9) at the continuum limit $\varepsilon \to 0$. The linear stability condition of the ExKS model has yet to be uncovered.

Importantly, the volcano effect is observed at the large adaptation-time regime $\tau = O(1/\varepsilon)$ when the stiffness is sufficiently large. The parameter regime and scaling for the volcano effect to take place under a given background chemical concentration was identified in the previous study [28]. The present result confirms that the same scaling property holds for the volcano effect even in the self-organized aggregation.

Furthermore, it is also uncovered that the variety of self-organized pattern formation occurs at large adaptation times when ε is moderate. More specifically, at $\varepsilon = 1$ [in Fig. 1(b)],

the standing and traveling bands are newly discovered at, respectively, $\tau = 10$ and $\tau = 100$. In the following subsections, we put more focus on the volcano effect and the standing and traveling bands.

B. Volcano Effect

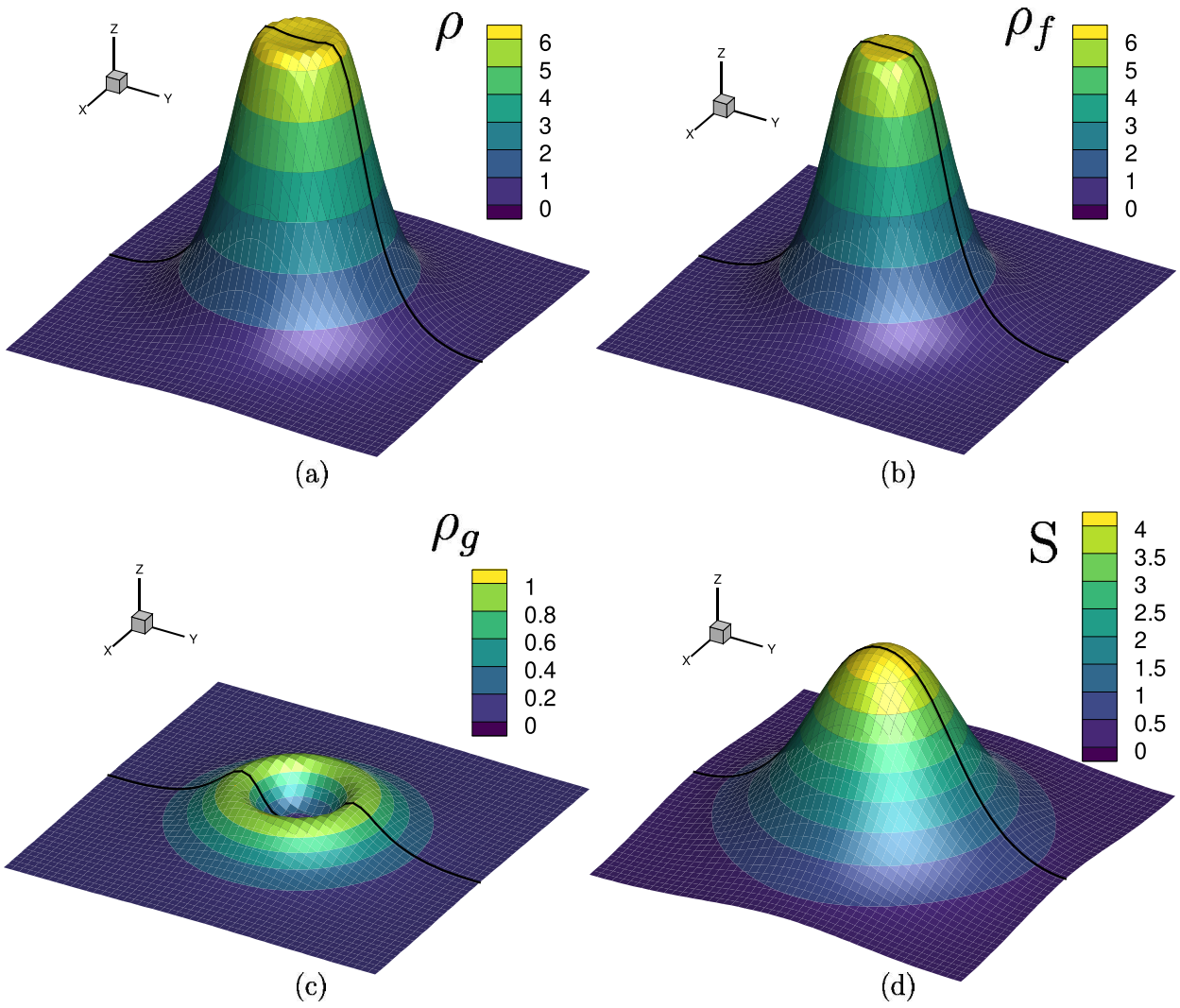

FIG. 2: Spatial distributions of the total population density ρ [in (a)], the population density of the running cells ρ_f [in (b)], the population density of the tumbling cells ρ_g [in (c)], and the concentration of chemical cue S [in (d)] at $\varepsilon = 0.1$, $\tau = 10$, $\delta = 0.01$, and $\chi = 0.9$. (Reprinted from Fig. 2 in Ref. [29].) The volcano effects are observed in ρ and ρ_g while ρ_f and S are unimodal. The intersections shown by solid lines are also shown in Fig. 4.

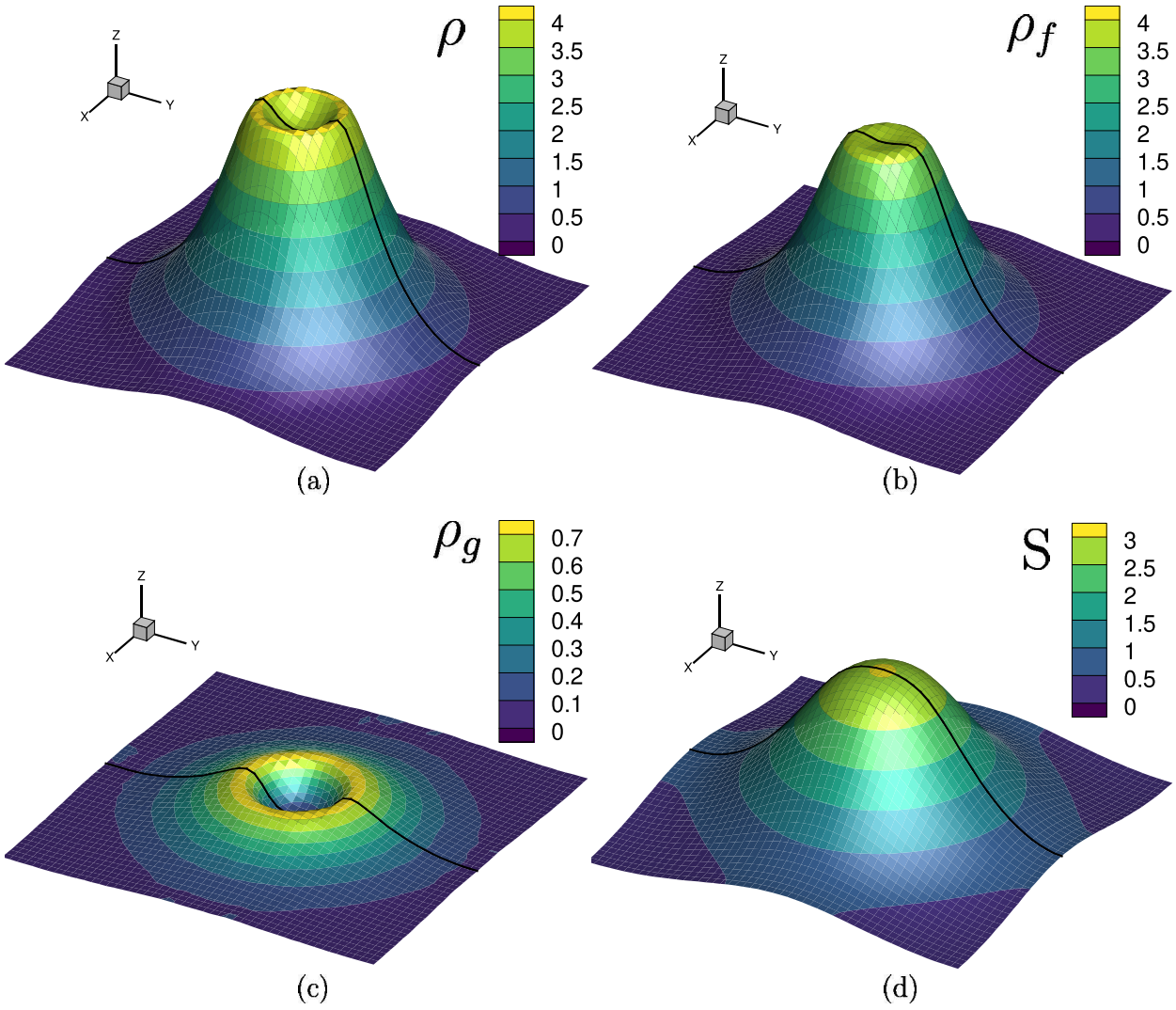

FIG. 3: Spatial distributions of the total population density ρ [in (a)], the population density of the running cells ρ_f [in (b)], the population density of the tumbling cells ρ_g [in (c)], and the concentration of chemical cue S [in (d)] at $\varepsilon = 1$, $\tau = 1$, $\delta = 0.01$, and $\chi = 0.9$. (Reprinted from Fig. 3 in Ref. [29].) The volcano effects are observed in ρ, ρ_f, and ρ_g while S is unimodal. The intersections shown by solid lines are also shown in Fig. 4

In the previous study [28], it was clarified that the volcano effect occurs under a given unimodal distribution of the chemical cue at the large adaptation-time scaling $\tau = O(1/\varepsilon)$. This study confirms that the volcano effect occurs even in the self-organized aggregation at the large adaptation-time scaling.

Figures. 2 and 3 show the spatial distributions of the total population density ρ, the population density of running cells ρ_f, the population density of tumbling cells ρ_g, and the

concentration of the chemical cue S at $\tau = 1/\varepsilon$ at, respectively, $\varepsilon = 0.1$ and $\varepsilon = 1$. The distributions at the cross sections shown by the solid black lines in each figure are also shown in Fig. 4.

It is seen that the volcano effect is observed in the total population density and the population density of the tumbling cells even though the concentration of the chemical cue is unimodal. From the comparison between the results with $\varepsilon = 0.1$ [Fig. 2] and $\varepsilon = 1$ [Fig. 3], it is seen that the volcano effect becomes more evident when ε becomes large. Moreover, the volcano effect is observed even in the population density of running cells ρ_f at $\varepsilon = 1$. We note that the volcano effect is never observed in ρ_f in MC simulations when ε is small, say $\varepsilon \lesssim 0.2$, although the volcano effect remains in ρ and ρ_g at the continuum limit at the large adaptation-time scaling. This observation is consistent with the numerical result obtained by the ExKS model, which is obtained by the asymptotic analysis of Eq. (9) at the continuum limit $\varepsilon \to 0$ (see also Fig. 4). To understand the enhancement of the volcano effect at moderate ε, the higher-order asymptotic analysis may be an important future study.

In Fig. 4, the intersections of the two-dimensional distributions of ρ, ρ_f, ρ_g, and S obtained at the large adaptation-time scaling $\tau = 1/\varepsilon$ at different values of ε are compared. Here, the result at the continuum limit $\varepsilon \to 0$ is obtained by the finite volume scheme of the ExKS model, which is the continuum-limit model derived by the asymptotic analysis of Eq. (9) at the large adaptation-time scaling $\tau = O(1/\varepsilon)$. It is seen that the volcano effect occurs in ρ and ρ_g while S is always unimodal. The results obtained at $\varepsilon = 0.1$ are well approximated by the ExKS model. These features are consistent with the results in the previous study.

C. Standing and Traveling Bands

The standing and traveling bands shown in the instability diagram at $\varepsilon = 1$ [Fig. 1(b)] are shown in, respectively, Figs. 5 and 6. In the figures, the flux $\vec{j}$ is calculated as

$$\vec{j}(t,x) = \int_{\mathrm{R}} < vf > (t,x,m)dm.$$

In Fig. 5 (a), it is seen that the local flux is almost zero, $|\vec{j}| \simeq 0$, so that both of the population density ρ and the concentration of chemical cue S are in the stationary state. It is also seen from Fig. 5 (b) that there is no phase difference between the bands of population

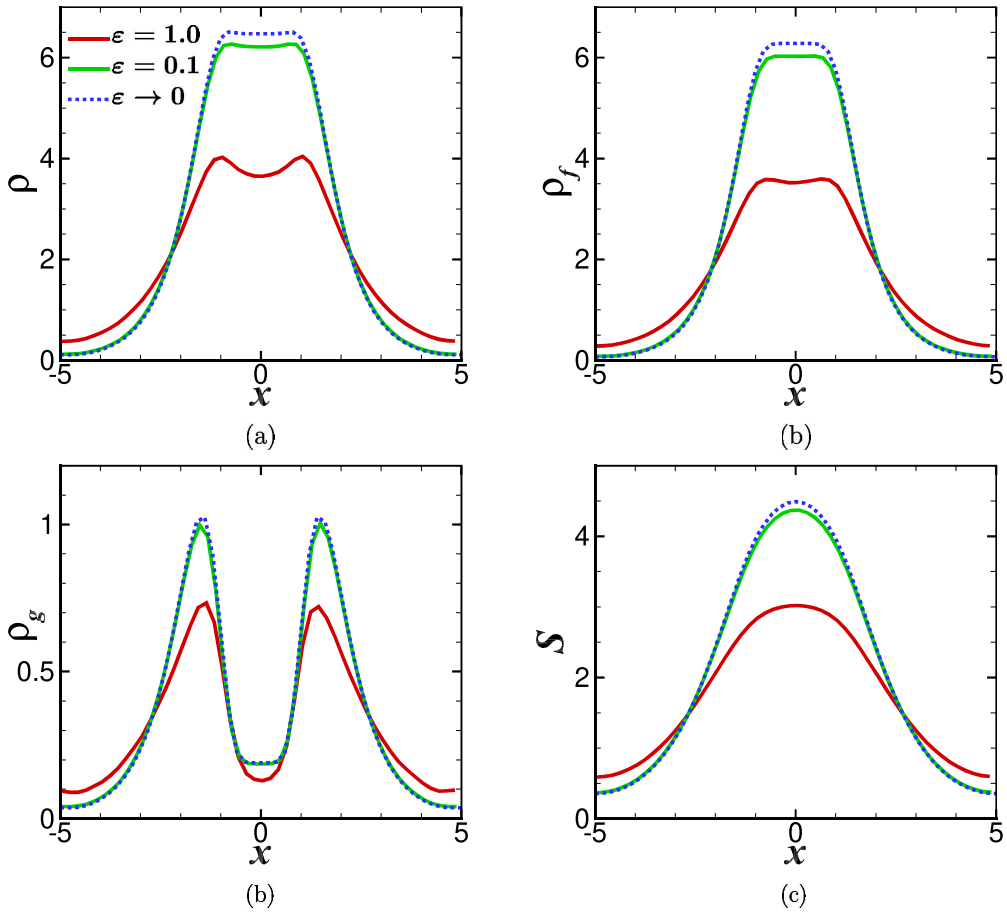

FIG. 4: Comparison of the total population density ρ [in (a)], the population density of running cells ρ_f [in (b)], the population density of tumbling cells ρ_g [in (c)], and the concentration of chemical cue S [in (d)] at different values of ε at the large adaptation time scaling $\tau = \beta/\varepsilon$ with $\beta = 1$. (Reprinted from Fig. 4 in Ref. [29].) The spatial distributions of the quantities at the intersections shown by solid lines in Figs. 2 and 3 are shown.

density ρ and concentration of chemical cue S.

On the other hand, in Fig. 6, a significant flux is observed on the band of the population density. The flow direction is perpendicular to the population band; that is, the traveling population band is created. Interestingly, in Fig. 6(b), a small phase difference is observed between the bands of population density ρ and concentration of chemical cue S. Moreover, the band of S is followed by the band of ρ. This result was unexpected because the chemical cue is produced by the bacteria, so that it seems to be natural that the band of chemical cue is followed by the population band. In this proceedings, we just report this interesting self-organized phenomena. To understand the mechanism of the self-organized traveling band a

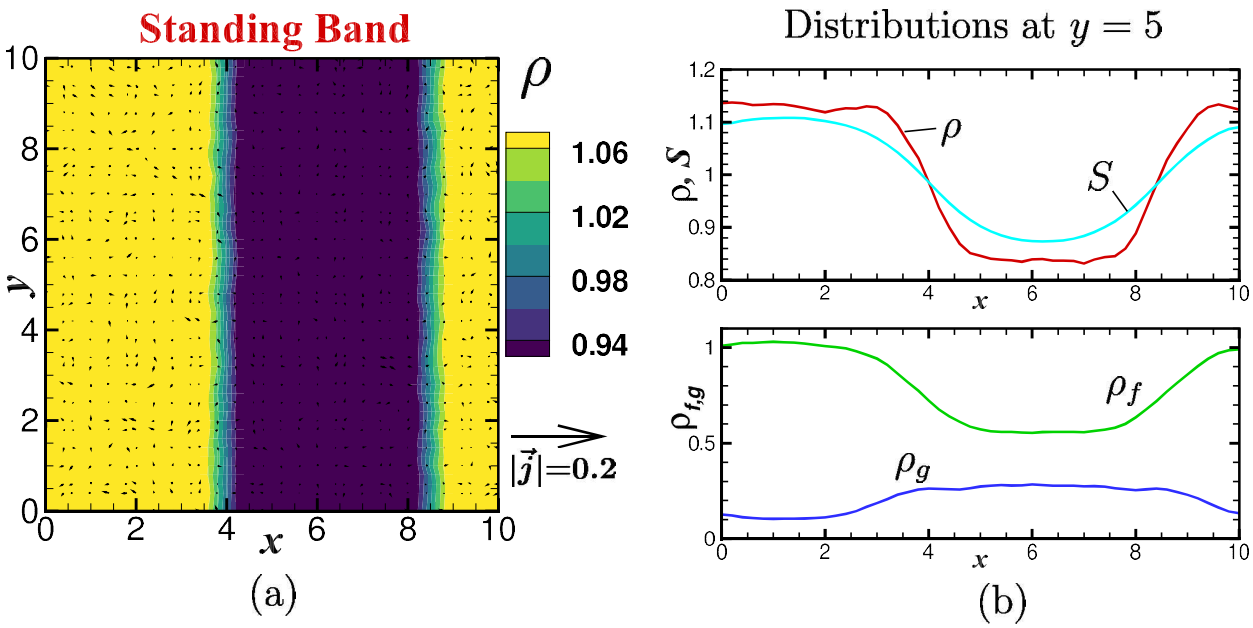

FIG. 5: Standing band observed at $\varepsilon = 1$, $\tau = 10$, $\chi = 0.7$, and $\delta = 0.01$. (Reprinted from Fig. 5 in Ref. [29].) Figure (a) shows the spatial distributions of the total population density ρ and the flux $\vec{j}$. Figure (b) shows the distributions of ρ, S, ρ_f, and ρ_g at the intersection $y = 5$ in figure (a).

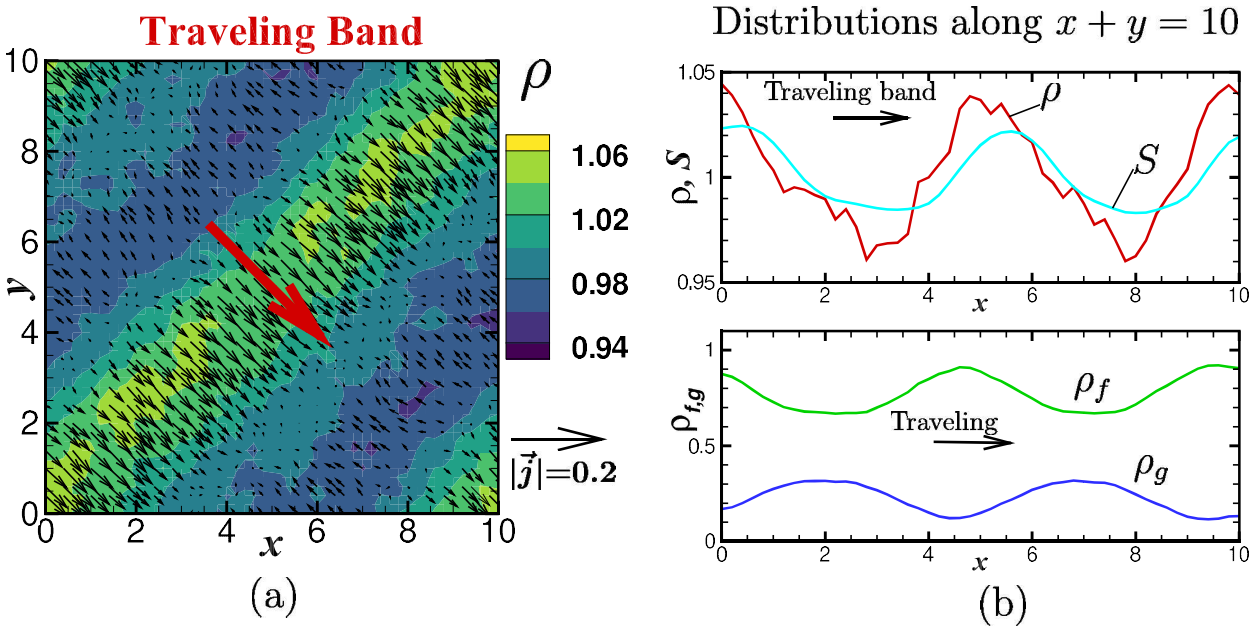

FIG. 6: Traveling band observed at $\varepsilon = 1$, $\tau = 100$, $\chi = 0.7$, and $\delta = 0.01$. (Reprinted from Fig. 6 in Ref. [29].) Figure (a) shows the spatial distributions of the total population density ρ and the flux $\vec{j}$. Figure (b) shows the distributions of ρ, S, ρ_f, and ρ_g along the diagonal $x + y = 10$ in figure (a).

further investigation is required.

V. CONCLUDING REMARKS

The self-organized pattern formation of run-and-tumble chemotactic bacteria in a periodic square domain is numerically investigated by the MC method of the kinetic transport equation (9) coupled with the reaction-diffusion equation of the chemical cue (14). The MC simulations are performed for a wide range of parameters of the stiffness of chemotactic response χ/δ and the internal adaptation time τ at two different values of the mean run length ε, i.e., $\varepsilon = 0.1$ and $\varepsilon = 1$.

The results of the pattern formation are summarized in the instability diagram, Fig. 1. Under the linear stability condition of the KS model, which is derived by the asymptotic analysis of the kinetic transport model at the small adaptation-time scaling $\tau = O(\varepsilon)$, the initial uniform states are always stable at both $\varepsilon = 0.1$ and $\varepsilon = 1$. At $\varepsilon = 0.1$, the linear stability condition is sharp even at large adaptation times, while at $\varepsilon = 1$, the self-organized aggregation is suppressed at large adaptation times.

The volcano effect is observed at the large adaptation-time scaling $\tau = (1/\varepsilon)$ when the stiffness of the chemotactic response is sufficiently large. The previous study [28] clarified that the volcano effect is generated under a given unimodal distribution of the chemical cue due to the coupling of diffusion, adaptation, and finite tumbling duration occurring at the large adaptation-time scaling. It was also numerically confirmed that the volcano effect remains even at the continuum limit $\varepsilon \to 0$ at the large adaptation-time scaling. This study confirms that the volcano effect occurs even in the self-organized aggregation, which is more relevant to the experimental situation. Furthermore, it is also clarified that the volcano effect is enhanced at the moderate value of ε (i.e., $\varepsilon = 1$).

Unexpectedly, at $\varepsilon = 1$, different types of pattern formations are discovered; that is, the standing and traveling bands are generated at very large adaptation times, i.e., $\tau = 10$ and $\tau = 100$, respectively. Remarkably, in the traveling band, the band of chemical cue is followed by the band of population density of the bacteria although the chemical cue is produced by the bacteria. Since we only considered the pattern formation in the (unrealistic) periodic square domain in this study, the experimental possibility of the self-organized traveling band may be questionable. We also only considered the uniform equilibrium solution

of the kinetic transport model as the initial data. It is not known if the pattern formation depends on the initial data. Finally, we remark that the physical relevance and the mathematical mechanism of the standing and traveling bands as well as the enhancement of the volcano effect, both occurring at moderate ε , should be an important topic for future study.

Appendix A: Derivation of the continuum-limit model

The continuum-limit models, which are utilized to compared with the MC results in the main text, were previously derived in literatures, e.g., Refs. [4, 7, 9, 17, 19, 25]. In this appendix, we briefly describe the derivation of the models for the completeness of this paper.

1. Small adaptation-time scaling

By following the procedure in Ref. [19], we change the variables of Eq. (17) as follows:

$$f_\varepsilon(t,x,v,m) = p_\varepsilon\left(t,x,v,y=\frac{M(S_\varepsilon)-m}{\varepsilon}\right), \quad g_\varepsilon(t,x,m) = q_\varepsilon\left(t,x,y=\frac{M(S_\varepsilon)-m}{\varepsilon}\right).$$

Then, we have

$$\varepsilon^2\partial_t p_\varepsilon + \varepsilon v\cdot\nabla_x p_\varepsilon + \partial_y\left\{\left(v\cdot G_\varepsilon - \frac{y}{\alpha}\right)p_\varepsilon\right\} = \mu q_\varepsilon - \Lambda(\varepsilon y)p_\varepsilon, \tag{A.1a}$$

$$\varepsilon^2\partial_t q_\varepsilon + \partial_y\left\{-\frac{y}{\alpha}q_\varepsilon\right\} = \Lambda(\varepsilon y) < p_\varepsilon > -\mu q_\varepsilon, \tag{A.1b}$$

where we write $G_\varepsilon = \nabla_x M(S_\varepsilon)$. By integrating the sum of the above equations with respect to v and y, we obtain the following conservation law:

$$\partial_t\rho_\varepsilon + \nabla_x\cdot\left(\frac{j_\varepsilon}{\varepsilon}\right) = 0, \tag{A.2}$$

where ρ_ε is the total population density, i.e., $\rho_\varepsilon = \rho_{p_\varepsilon} + \rho_{q_\varepsilon}$ with $\rho_{p_\varepsilon} = \int < p_\varepsilon > dy$ and $\rho_{q_\varepsilon} = \int q_\varepsilon y$, and the flux j_ε is defined as

$$j_\varepsilon = \int < vp_\varepsilon > dy. \tag{A.3}$$

As can be seen below, the KS equation is obtained from Eq. (A.2) at the continuum limit ($\varepsilon \to 0$).

We assume p_ε and q_ε are compactly supported with respect to y and $\Lambda(\varepsilon y)$ in Eq. (A.1) can be expanded as $\Lambda(\varepsilon y) = 1 + \varepsilon\Lambda'(0)y + O(\varepsilon^2)$. Then, from the leading-order terms of Eq. (A.1), we obtain the leading-order equation as follows:

$$\partial_y \left\{ \left(v \cdot G_0 - \frac{y}{\alpha} \right) p_0 \right\} = \mu q_0 - p_0, \tag{A.4a}$$

$$\partial_y \left\{ -\frac{y}{\alpha} q_0 \right\} = < p_0 > -\mu q_0. \tag{A.4b}$$

By integrating each of Eqs. (A.4) w.r.t y, we obtain the following relation between the leading-order population densities:

$$\int p_0 dy = \mu \rho_{q_0} = \rho_{p_0} = \frac{\mu}{1+\mu} \rho_0. \tag{A.5}$$

Furthermore, by taking the moment of the above equation multiplied by v, we obtain the flux j_0 as follows:

$$j_0 = \int < v p_0 > dy = 0. \tag{A.6}$$

From the first-order terms of Eq. (A.1), we have the equation as follows:

$$\nabla_x \cdot (v p_0) + \partial_y \left\{ \left(v \cdot G_0 - \frac{y}{\alpha} \right) p_1 \right\} + \partial_y (v \cdot G_1 p_0) = \mu q_1 - p_1 - \Lambda'(0) y p_0, \tag{A.7a}$$

$$\partial_y \left\{ \left(-\frac{y}{\alpha} \right) q_1 \right\} = < p_1 > -\mu q_1 + \Lambda'(0) y < p_0 > . \tag{A.7b}$$

By integrating the sum of above equations multiplied by v with respect to v and y, we obtain

$$\nabla_x \cdot \int < v \otimes v p_0 > dy = -j_1 - \Lambda'(0) \int y < v p_0 > dy,$$

$$\frac{\mu}{1+\mu} c_d \nabla_x \rho_0 = -j_1 - \Lambda'(0) \int y < v p_0 > dy,$$

where we use Eq. (A.5) and $< v \otimes v >= c_d I$ with $c_d = 1/d$ for $d = 1, 2, 3$. Here, I is the identity matrix. The last term of the above equation is obtained by integrating Eq. (A.4a) multiplied by vy with respect to v and y:

$$-\int y \partial \left\{ < v \otimes v p_0 > \cdot G - \frac{y}{\alpha} < v p_0 > \right\} dy = \int y < v p_0 > dy,$$

$$\int < v \otimes v p_0 > dy \cdot G - \frac{1}{\alpha} \int y < v p_0 > dy = \int y < v p_0 > dy,$$

$$\int y < v p_0 > dy = \frac{\mu}{1+\mu} \frac{\alpha}{1+\alpha} c_d \rho_0 G.$$

Hence, the flux j_1 is written as follows:

$$j_1 = -\frac{\mu}{1+\mu} c_d \left[\nabla_x \rho_0 + \frac{\alpha}{1+\alpha} \Lambda'(0) G \rho_0 \right]. \tag{A.8}$$

Thus, by taking the limit $\varepsilon \to 0$ at Eq. (A.2), we obtain the KS equation (18).

2. The Extended Keller-Segel model

The derivation of Eq. (22) is as follows. In the following, we write the average of f_ε over the velocity space as $A_\varepsilon =< f_\varepsilon >$.

From the leading-order terms of Eq. (21), we can write the leading-order solution as follows:

$$f_0 = A_0(t,x,m), \quad g_0 = \frac{\Lambda(M_0-m)}{\mu}A_0(t,x,m). \tag{A.9}$$

Here, $A_0(t,x,m)$ is an unknown function independent of the velocity v.

From the ε^1 terms of Eq. (21), we obtain

$$v\cdot\nabla_x A_0 = \mu g_1 - \Lambda(M_0-m)f_1 - \Lambda'(M_0-m)M_1A_0, \tag{A.10a}$$

$$0 = \Lambda(M_0-m)A_1 + \Lambda'(M_0-m)M_1A_0 - \mu g_1. \tag{A.10b}$$

By taking the sum of the above equations, we obtain the following equation,

$$v\cdot\nabla_x A_0 = \Lambda(M_0-m)(A_1-f_1).$$

Hence, f_1 can be written in the form

$$f_1 = A_1(t,x,m) + v\cdot B_1(t,x,m), \tag{A.11a}$$

with

$$B_1 = -\frac{\nabla_x A_0}{\Lambda(M_0-m)}. \tag{A.11b}$$

From Eq. (A.10b), we can also write g_1 as follows:

$$g_1 = \frac{1}{\mu}\left(\Lambda(M_0-m)A_1 + \Lambda'(M_0-m)M_1A_0\right). \tag{A.12}$$

Subsequently, from the ε^2 terms of Eq. (21), we obtain the equation as follows:

$$\begin{aligned}\partial_t A_0 + v\cdot\nabla_x(A_1+v\cdot B_1) + \partial_m\left\{\left(\frac{M_0-m}{\beta}\right)A_0\right\} &= \mu g_2 - \Lambda(M_0-m)f_2\\ -\Lambda'(M_0-m)M_1(A_1+v\cdot B_1) - \frac{1}{2}\Lambda''(M_0-m)M_2A_0,&\end{aligned} \tag{A.13a}$$

$$\begin{aligned}\frac{\Lambda(M_0-m)}{\mu}\partial_t A_0 + \partial_m\left\{\left(\frac{M_0-m}{\beta}\right)\frac{\Lambda(M_0-m)}{\mu}A_0\right\} &= \Lambda(M_0-m)A_2 - \mu g_2\\ +\Lambda'(M_0-m)M_1A_1 - \frac{1}{2}\Lambda''(M_0-m)M_2A_0.&\end{aligned} \tag{A.13b}$$

By integrating the sum of the above equations with respect to v, we obtain the equation to determine the leading-order solution A_0 as follows:

$$\left(1+\frac{\Lambda(M_0-m)}{\mu}\right)\partial_t A_0+\nabla_x\cdot(c_d B_1)+\partial_m\left\{\left(\frac{M_0-m}{\tau}\right)\left(1+\frac{\Lambda(M_0-m)}{\mu}\right)A_0\right\}=0. \tag{A.14}$$

When we write the total density of cells with an internal state m as $h_0 =< f_0 > +g_0$, i.e., from Eq. (A.9),

$$h_0(t,x,m)=\left(1+\frac{\Lambda(M_0-m)}{\mu}\right)A_0(t,x,m), \tag{A.15}$$

we can rewrite Eq. (A.14) as follows:

$$\partial_t h_0+\nabla_x\cdot(c_d B_1)+\partial_m\left\{\left(\frac{M_0-m}{\tau}\right)h_0\right\}=0, \tag{A.16a}$$

with

$$B_1=-\frac{1}{\Lambda(M_0-m)}\nabla_x\left(\frac{h_0}{1+\frac{\Lambda(M_0-m)}{\mu}}\right). \tag{A.16b}$$

Thus, we obtain the ExKS model (22).

---

[1] Berg, H., Brown, D.: Chemotaxis in escherichia coli analysed by three-dimensional tracking. Nature **239**(5374), 500–504 (1972)

[2] Calvez, V.: Chemotactic waves of bacteria at mesoscale. Journal of European Mathematical Society **22**(2), 593–668 (2020)

[3] Calvez, V., Perthame, B., Yasuda, S.: Traveling wave and aggregation in a flux-limited keller-segel model. Kinetic and Related Models **11**(4), 891–909 (2018)

[4] Chalub, F., Markowich, P., Perthame, B., C., S.: Kinetic models for chemotaxis and their drift-diffusion limits. Monatsh. Math. **142**, 123–141 (2004)

[5] Dolak, Y., Schmeiser, C.: Kinetic models for chemotaxis: Hydrodynamic limits and spatio-temporal mechanisms. J. Math. Biol. **51**, 595–615 (2005)

[6] Emako, C., Gayrard, C., Buguin, A., Almeida, N., Vauchelet, N.: Traveling pulses for a two-species chemotaxis model. PLoS Computational Biology **12**(4) (2016)

[7] Erban, R., Othmer, H.: From individual to collective behaviour in bacterial chemotaxis. SIAM J. Appl. Math. **65**(2), 361–391 (2004)

[8] G., H.: Bacterial chemotaxis: the early years of molecular studies. Annu. Rev. Microbiol **66**, 285–303 (2012)

[9] Hillen, T., Othmer, H.: The diffusion limit of transport equations derived from velocity jump processes. SIAM J. Appl. Math. **61**(3), 751–775 (2000)

[10] Kalinin, Y.V., Jiang, L., Tu, Y., Wu, M.: Logarithmic sensing in escherichia coli bacterial chemotaxis. Biophys J. **96**(6), 2439–2448 (2009)

[11] Kanzler, L., Schmeiser, C., Tora, V.: Two kinetic models for non-instantaneous binary alignment collisions (2023). Kinet. Relat. Models DOI 10.3934/krm.2023038.

[12] Keller, E., Segel, L.: Initiation of slime mold aggregation viewed as an instability. J. Theor. Biol. **26**, 399–415 (1970)

[13] Keller, E., Segel, L.: Model for chemotaxis. J. Theor. Biol. **30**, 225–234 (1971)

[14] Turner, L., Ryu, W., Berg, H.: Real-Time Imaging of Fluorescent Flagellar Filaments. Journal of Bacteriology **182**(10), 2793–2801 (2000).

[15] Mittal, N., Budrene, E., Brenner, M., Van Oudenaarden, A.: Motility of escherichia coli cells in clusters formed by chemotactic aggregation. Proceedings of the National Academy of Sciences of the United States of America **100**(23), 13259–13263 (2003)

[16] Othmer, H., Dunbar, S., Alt, W.: Models of dispersal in biological systems. Journal of Mathematical Biology **26**(3), 263–298 (1988)

[17] Perthame, B. and Tang, M. and Vauchelet, N.: Derivation of the bacterial run-and-tumble kinetic equation from a model with biological pathway Journal of Mathmatical Biology **73**, 1161–1178 (2016)

[18] Perthame, B. and Sun, W. and Tang, M.: The fractional diffusion limit of a kinetic model with biochemical pathway. ZEITSCHRIFT FUR ANGEWANDTE MATHEMATIK UND PHYSIK, **69**(3), 67 (2018).

[19] Perthame, B., Sun, W., Tang, M., Yasuda, S.: Multiple asymptotics of kinetic equations with internal states. Mathematical Models and Methods in Applied Sciences **30**(06), 1041–1073 (2020)

[20] Perthame, B., Yasuda, S.: Stiff-response-induced instability for chemotactic bacteria and flux-limited Keller-Segel equation. Nonlinearity **31**(9), 4065–4089 (2018)

[21] Saragosti, J., Calvez, V., Bournaveas, N., Perthame, B., Buguin, A., Silberzan, P.: Directional persistence of chemotactic bacteria in a traveling concentration wave. Proceedings of the

National Academy of Sciences **108**(39), 16235–16240 (2011)

[22] Simons, J., Milewski, P.: The volcano effect in bacterial chemotaxis. Mathematical and Computer Modelling **53**(7-8), 1374–1388 (2011)

[23] Spiro, P., Parkinson, J., Othmer, H.: A model of excitation and adaptation in bacterial chemotaxis. Proceedings of the National Academy of Sciences **94**(14), 7263–7268 (1997)

[24] Tu, Y., Shimizu, T., Berg, H.: Modeling the chemotactic response of escherichia coli to time-varying stimuli. Proceedings of the National Academy of Sciences **105**(39), 14855–14860 (2008)

[25] Xue, X., Xue, C., Tang, M.: The role of intracellular signaling in the stripe formation in engineered escherichia coli populations. PLoS Computational Biology **14**(6) (2018)

[26] Yasuda, S.: Monte carlo simulation for kinetic chemotaxis model: An application to the traveling population wave. Journal of Computational Physics **330**, 1022 – 1042 (2017)

[27] Yasuda, S.: Effects of internal dynamics on chemotactic aggregation of bacteria. Physical Biology **18**(6), 066001 (2021)

[28] Yasuda, S.: Numerical study of the volcano effect in chemotactic aggregation based on a kinetic transport equation with non-instantaneous tumbling. Bulletin of Mathematical Biology **84**, 113 (2022).

[29] Adachi, K., Yasuda, S.: Numerical study on the self-organized pattern formation of run-and-tumble chemotactic bacteria. Springer Proceedings in Mathematics & Statistics **429**, 235–248 (2023).